

Chemically-Sensitive Accessibility Study of Porous Materials at the Single Particle Level as Evaluated within a Multiplexed Microfluidic Chip with Fluorescence Microscopy

Alessia Broccoli,^{1,3} Luca Carnevale,^{1,2,3} Rafael Mayorga González,^{1,2,3} Joren M. Dorresteyn,² Bert M. Weckhuysen,² Wouter Olthuis,¹ Mathieu Odijk,¹ and Florian Meirer,^{2,*}

¹BIOS Lab on a Chip Group, MESA+ Institute for Nanotechnology, Max Planck Center for Complex Fluid Dynamics, University of Twente, Drienerlolaan 5, 7522 NB Enschede

²Inorganic Chemistry and Catalysis Group, Debye Institute for Nanomaterials Science and Institute for Sustainable and Circular Chemistry, Utrecht University, Universiteitsweg 99, 3584 CG Utrecht

³These authors contributed equally.

*Lead contact and Correspondence: f.meirer@uu.nl

SUMMARY

Understanding the mass transfer phenomena taking place in solid catalysts, batteries, fuel cells, and adsorbents is essential to improve their performances. Uptake experiments of ultraviolet-active or fluorescent probes represent a direct way to directly provide an accessibility measure of porous particles. We propose a new method to evaluate the accessibility of functional porous materials at the single-particle level. A multiplexed polydimethylsiloxane microfluidic device and a fluorescence microscope are employed to assess the uptake of fluorescent molecules in porous particles over time. The device allows for performing multiple uptake experiments in parallel, enabling the comparison of different particles under the same conditions. We showcase the method by studying the diffusion and adsorption properties of a dye in different silica model particles. The approach allows for probing interparticle heterogeneity in accessibility and accessible surface area as well as the dependence of these parameters on electrostatic interactions between the particle and the probe molecules.

KEYWORDS

Mass transfer, accessibility, single-particle characterization, microfluidics, uptake experiments

THE BIGGER PICTURE

Porous materials find use in diverse industrial applications, from catalysis to environmental remediation. To improve their performance, tools for their precise characterization are required. This includes investigating mass transfer phenomena taking place therein, along with the interactions between the guest molecules and the host material pore walls. In this work, we introduce a microfluidic-based method for direct assessment of functional porous particles' accessibility. Using fluorescent probes, we monitor and quantify the uptake of molecules within individual porous particles over time, capturing dynamic processes and heterogeneities often not visible when using traditional bulk techniques. By facilitating real-time, single-particle analysis in a detailed and controlled fashion, our method shows great potential to unravel the mechanisms governing mass transport in porous solids.

INTRODUCTION

Molecular transport is a key aspect in the applications of most functional porous materials, as it determines their performances as adsorbents, batteries, fuel cells, and solid catalysts¹. The efficiency of these materials depends on diffusion, adsorption, and desorption processes taking place inside their pores, which are in turn influenced by the physicochemical interactions between the pore walls and guest molecules¹⁻⁴. Therefore, understanding these phenomena is essential for designing functional materials with much improved performances.

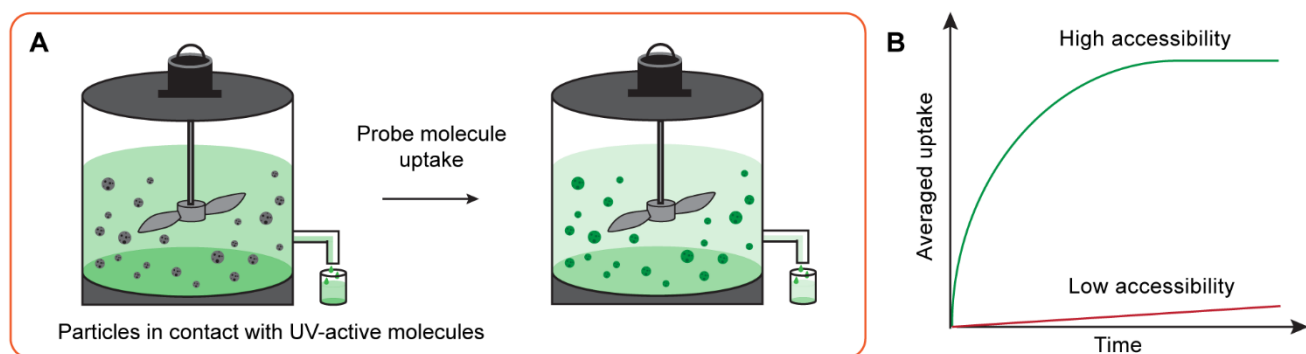
A direct way for elucidating mass transfer processes in porous materials is based on uptake and release experiments of ultraviolet (UV)-active^{5,6} or fluorescent probes, directly providing a pore accessibility measure (i.e., how easily molecules enter the porous host). One example of such an approach is offered by the so-called Akzo Nobel Accessibility Index (AAI) test^{4,7,8} introduced for Fluid Catalytic Cracking (FCC) particles, which is also used industrially. The method is based on measuring the uptake of UV-active molecules into catalyst particles by tracking the relative concentration of the molecules in solution over time (Figures 1A and 1B), providing a relative measure of the penetration rate. In this approach, it is assumed that the behavior of the entire system replicates the one of an individual particle. However, structural and compositional differences exist within a catalyst batch^{9,10}, that cannot be captured by ensemble-averaged analytical measurements.

Characterizing the uptake process of individual particles would be beneficial to supplement the data obtained from bulk methods, and also to capture heterogeneities among particles. This has been tried with different techniques. Recently, confocal laser scanning microscopy (CLSM) has proven to be a useful tool for visualizing the inner structure of materials. It has been applied to monitor the uptake and distribution of dyes¹¹⁻¹⁴ and dye-labeled particles^{15,16} on the single-particle scale. The approach allowed a direct visualization of the particle's accessible porosity and the correlation between its structure and activity. This provides useful insight for the design of more efficient materials. Moreover, microimaging techniques based on interference microscopy (IFM) and IR microscopy (IRM)^{2,17,18} were successfully used for recording the evolution of guest molecule distributions in nanoporous host materials. Furthermore, advanced electron¹⁹⁻²⁵ and X-ray²⁶⁻³¹ microscopy techniques, have been applied to (partially) map the pore volume of individual particles in 3 dimensions and simulate mass transfer within them.

The mentioned analytical measurements require expensive equipment and sample preparation, and some of them are unfortunately destructive particularly due to the potential for ion, electron, and X-ray beam damage, as observed in electron microscopy and synchrotron-based techniques^{9,32,33}. Furthermore, the number of particles that can be studied with these methods is very limited. Recently, microfluidic devices have been used to characterize catalysts at the single particle level in a high throughput fashion by isolating catalyst particles based on their activity³⁴ and metal loading³⁵. However, this kind of approach has not yet been used to study intra-particle mass transport.

Here we propose a fast, cheap, and reproducible method (Figures 1C and 1D) to compare accessibility between and within different porous particles in a high throughput fashion. We used only a polydimethylsiloxane (PDMS) multiplexed microfluidic device and a LED-illuminated wide-field fluorescence microscope and we imaged and compared the uptake of fluorescent molecules by individual mesoporous silica particles. Moreover, we performed experiments using different solution conditions, to evaluate the influence of electrostatic interactions between guest molecules and host material on the overall uptake process. Furthermore, by suppressing these interactions the measured accessibilities were – for the tested samples – able to probe pore size accurately, obtaining a distribution comparable to the results from the N₂ physisorption method. Additionally, the saturation values of the uptake curves allowed us to study changes in accessible surface area as a function of guest-host interactions of individual particles, which cannot be distinguished with bulk and non-chemically sensitive techniques, such as gas physisorption. Finally, we investigated through simulations how internal diffusion, adsorption, and external mass transfer affected the shape of the uptake curves.

Bulk method



Single-particle method

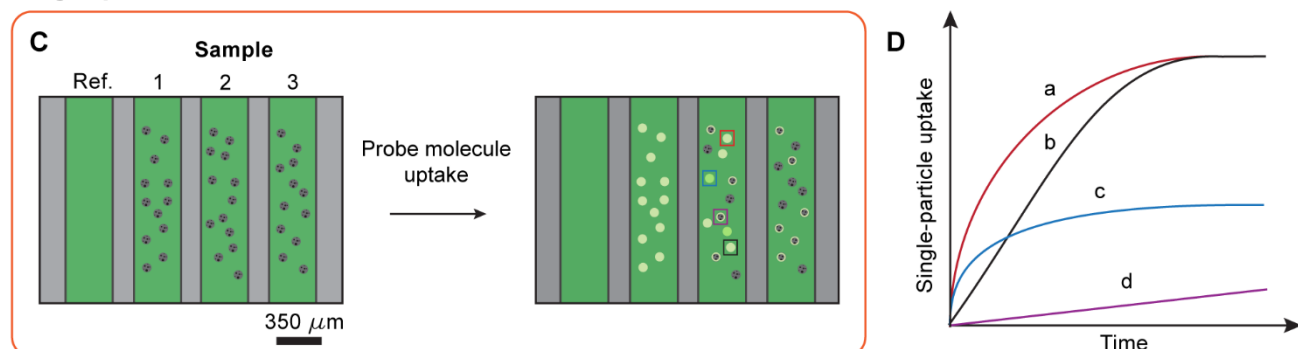


Figure 1 Schematic representation of the experimental methods to evaluate the accessibility of particles in bulk and at the single particle level. **A)** A stirred tank contains both UV-active molecules and porous particles. The concentration in the solution decreases due to the uptake of the porous material. **B)** Based on the concentration change, the bulk uptake [mol/g(material)] is computed and used to characterize the material's accessibility. **C)** A multiplexed microfluidic device containing 4 chambers is filled with porous particles and a liquid containing a fluorescent dye. One reference chamber (left) is left empty to control for photobleaching. As fluorescent molecules enter the porous particles, their fluorescence increases. **D)** The fluorescence of individual particles (in the highlighted squares) is tracked over time to assess the uptake of fluorophores and in turn the accessibility of individual particles. Curves a and b correspond to particles with the same accessible adsorption capacity (both curves plateau at the same value), but different accessibilities ($a > b$). Particle c is rather accessible (saturation is reached quickly) but the total uptake of fluorophores is less than in particles a and b. Particle d corresponds to a particle with very low accessibility (saturation is not reached during the time of the experiment).

The experiments were performed using microfluidic devices consisting of two PDMS layers, and a glass slide (Figure S1), as previously reported^{36,37}. The top layer contains four chambers, which allow the performance of three experiments in parallel under the same conditions while keeping a reference chamber to control for photobleaching (Figure 1C). In the experiments, each chamber is loaded with various porous SiO₂ particles. Then, all chambers are filled with water to first fill pores of the hydrophilic material by capillary forces, this process takes place in less than a second³⁸. Finally, the chambers are filled with a fluorescent dye solution. The mean fluorescence intensity, as a measure of dye concentration in each particle, is tracked individually as a function of time resulting in individual uptake curves (Figure 1D) constructed from the experimental data using a self-developed Matlab™ code. One can get information from the following features of these curves: 1) the final value of the curve contains information about the saturation state of the particle. If it is flat, the equilibrium in the uptake process has been reached (i.e., the particle surface is saturated with dye and there is no concentration change in the particle pore volume, Figure S2). Otherwise, uptake is still ongoing. 2) The intensity value reached after saturation contains information about the adsorption properties of the system. The higher this value, the more adsorption took place, which can be related to the surface area of the material. 3) The shape of the curve, i.e., how the curve's slope changes over time, contains information about the accessibility of the particle. The steeper the slope, the faster saturation is reached, and the more accessible the particle is.

THEORETICAL BACKGROUND

The interpretation of uptake data can be divided into two categories, based on the adsorption or diffusion as rate-limiting step. The latter represents the most common case for macroscopic adsorbent materials^{39,40}. Several models have been developed to

describe the experimentally obtained uptake curves⁴¹. However, most of these models require reaching a saturation state to extract the relevant parameters. The so-called intra-particle diffusion model⁴² does not have this requirement and is therefore widely used for slow uptake experiments. Here the fractional uptake $q(t)$ usually expressed in mg(probe)/g(solid) is plotted as a function of $t^{0.5}$ ^{43,44,53–58,45,63–67,46–52}.

At low saturation values with an ideal mixing of the liquid phase (i.e., the dye concentration in solution is constant in space), this would initially result in a linear curve that eventually reaches a plateau, representing saturation of the sorbent material (Figure 2A). In the case of prominent external mass transfer effects (no ideal mixing), a stagnant layer, i.e. a concentration gradient in the vicinity of the particle, is formed during uptake, slowing it down and resulting in a non-linear regime for small time values^{62,61} (Figure 2B). Typically, linear regression is performed on the linear part of the uptake curve (Eq. 1) and its slope is used to quantify the so-called intra-particle diffusion rate constant⁶⁸ K_p (mg/g min^{0.5}), which we refer to as accessibility index:

$$q(t) = K_p t^{0.5} + C_y \quad (1)$$

The y-intercept C_y (mg/g) is typically used to evaluate the extent of the boundary layer thickness and therefore the external mass transfer effects. When the fitted line passes through the origin, the external mass transport is negligible. Otherwise, a non-zero y-intercept value indicates a relevant contribution of the boundary layer effects to the measured intra-particle diffusion. Both positive^{43,44,53–58,45–52} and negative^{59–62} C_y values have been reported in the literature. Positive values are interpreted as fast adsorption by the material; thus, it is not possible to capture the actual starting point of the adsorption process. Negative values are related to a diffusion process retarded by the boundary layer effects. Moreover, some studies use the intercept of the fitted line with the x-axis to evaluate external mass transfer effects^{63–67}. Therefore, the exact physical meaning of the C_y parameter proposed in the aforementioned model remains unclear.

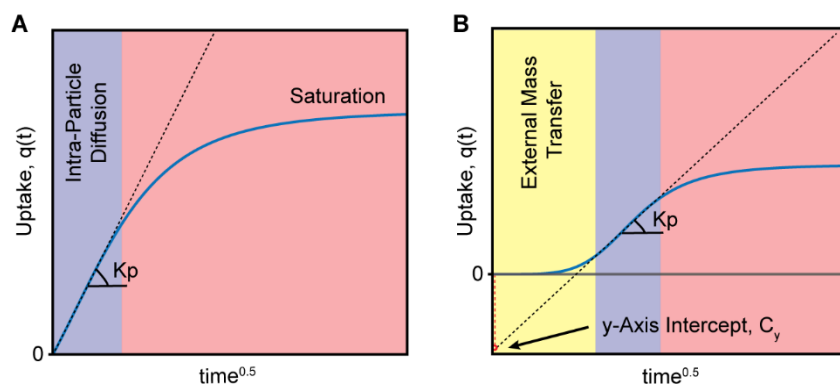


Figure 2 **A)** Ideal uptake curve with purely intraparticle diffusion and **B)** with external mass transfer contribution.

To investigate the significance of the accessibility index K_p and the y-intercept C_y , uptake simulations were performed by solving Fick's second law with the finite difference method. In our model (SI 2), no flux at the center of the particle and external mass transfer effects at the particle surface were included in the boundary conditions. Moreover, adsorption was considered to be much faster than the diffusion process, which established diffusion to be the rate-limiting step. As a result, local equilibrium between the diffusing and adsorbed substance can be postulated. To simplify, we assumed a linear dependence between the concentration of the free and adsorbed substance.

The molecular uptake in porous particles is mostly dominated by three parameters: 1) the internal particle diffusion coefficient D (m²/s), which increases with the pore size and pore interconnectivity; 2) the external mass transfer coefficient k (m/s), which depends on diffusion and convection outside the particle and correlates positively with D (SI 2, Eq. 7); and 3) the adsorption coefficient R (unitless proportionality constant expressing the ratio between adsorbed concentration and concentration in solution, SI 2, Eq. 2). The latter depends on the wall-molecule interactions as well as the number of accessible adsorption sites.

We performed a sensitivity analysis (Figure 3) to assess how these three parameters affect the uptake curve shape and its parameters K_p and C_y . Increasing the internal diffusion coefficient D of the particle resulted in a higher slope of the linear part of the uptake, i.e., higher accessibility index K_p , and a more negative y-axis intercept C_y (Figures 3A and 3D). A similar effect on K_p is observed by increasing k (reducing the external mass transfer limitations). However, it also shifts the linear regime of the uptake curve to shorter times, which results in a less negative y-intercept (Figures 3B and 3E). Finally, increasing the adsorption coefficient R increases the accessibility index K_p and decreases the y-intercept C_y (Figures 3C and 3F). It is worth noting that the external mass transfer coefficient k and the effective diffusion coefficient $D' = \frac{D}{1+R}$ which includes adsorption, are positively correlated due to the boundary conditions equating flow at the two sides of the solid-liquid interphase (SI 2, Eq. 7). Hence, increasing the

internal particle diffusion coefficient D will result in higher external mass transport (higher k) and vice-versa. However, both parameters contribute differently to the y-axis intercept C_y . Since the y-axis intercept is determined by several parameters, it should not be used to evaluate external mass transfer only.

In an uptake experiment, while using particles of the same material and pore volume, but different pore sizes, one varies the internal diffusion coefficient D and therefore the external mass transfer coefficient k as well as the adsorption coefficient R (as different surface areas are obtained). All of these values correlate positively with the amount of adsorbed material (uptake, $q(t)$) and the accessibility index K_p . Interestingly our experimental results show that the accessibility index and the y-axis intercept are correlated (Figure S3), proving the redundancy of using both parameters to characterize porous materials. Therefore, we will provide only the accessibility index K_p values obtained in the experiments to characterize and compare the processes.

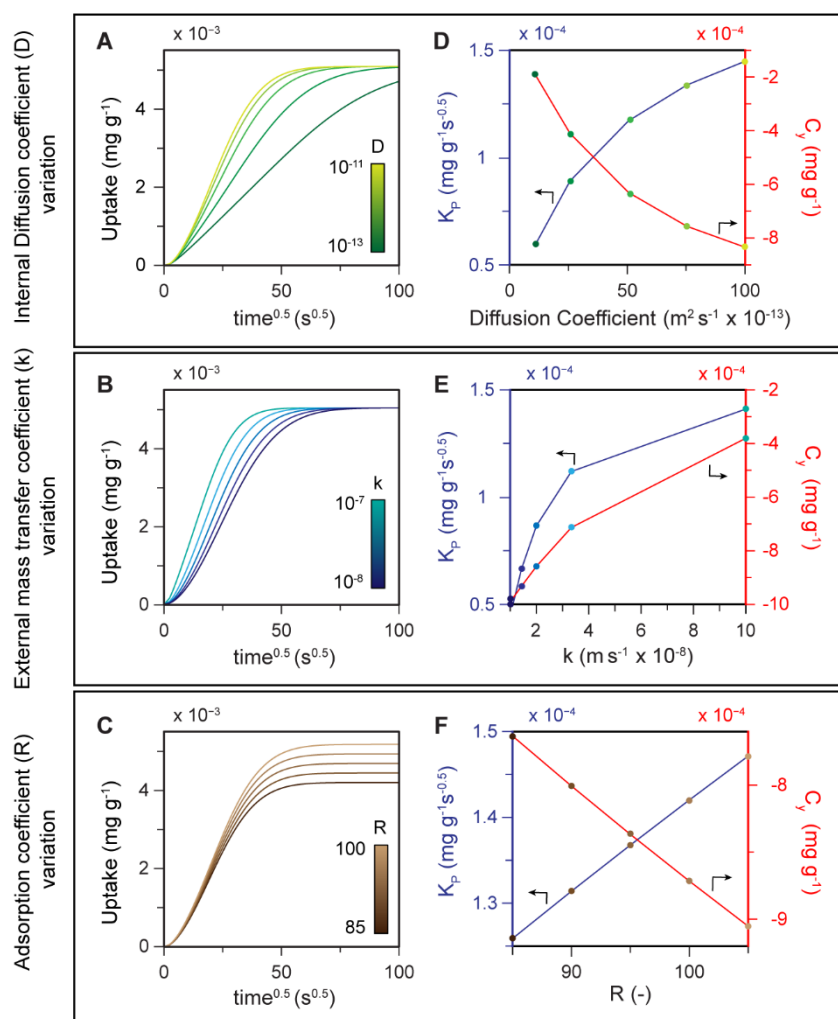


Figure 3 Uptake simulations obtained considering a 35 μm spherical particle. **A)** Uptake curves obtained changing the internal diffusion coefficient D ($k = 10^{-8}$ m/s and $R = 100$) **B)** the external mass transfer coefficient k ($D = 10^{-12}$ m²/s and $R = 100$) and **C)** the adsorption coefficient R ($D = 10^{-12}$ m²/s and $k = 10^{-8}$ m/s). **D), E),** and **F)** show the slopes (accessibility indices) and y-intercepts of the inflection point tangents of the uptake curves shown in **A), B),** and **C)** respectively.

RESULTS AND DISCUSSION

To showcase the developed method, we used SiO_2 particles with almost monodisperse pore size distributions (i.e., 50 nm, 35 nm, and 23 nm) (Figure 5A and SI 4) often used as catalyst supports (e.g., olefin polymerization catalysis). Rhodamine 110 (Rh110) (Figure 5B) was used as a fluorescent probe due to its photostability^{69,70}, high quantum yield, and fluorescent intensity being proportional to its concentration (Figure S5). Therefore, particle fluorescent intensity values were directly used to obtain the uptake curves (see SI 6), and the accessibility index was defined in $\text{min}^{0.5}$ units. The particles were placed in the chambers leaving one empty that was used as a reference to check the photostability of the dye (Figure 1C). Uptake experiments were conducted for 5 h and images were acquired every minute. Figures 4A and 4B display a cropped version of the fluorescence microscopy

images recorded at the beginning and end of the experiments using 50 nm pore-size particles showing an overall, but heterogeneous increase in intensity. Some particles of similar size display an intensity (i.e., concentration) gradient within them, whereas others show a more homogeneous dye distribution, hinting toward different pore connectivity. The final mean fluorescence intensity of the particles resulted higher than in the bulk solution, due to the adsorption of the probe molecules in the pore structure. Figure 4C shows the mean intensities of particles of the same sample as a function of time (the initial intensity of each particle was subtracted). Even particles that belong to the same batch, differ strongly in their uptake curves and therefore accessibilities. Traditional bulk experiments could not have measured this, which highlights the importance of the proposed method for elucidating inter-particle heterogeneity. Plotting the same uptakes versus $t^{0.5}$ results in a sigmoid-like (asymmetric sigmoid) curve (Figure 4D). The non-linear beginning of the curve suggests external mass transfer limitations. That is, a concentration gradient is formed outside the particle that slows the internal diffusion down. Moreover, the fact that the curves are reaching a plateau, means that, as expected, at some point in time the particles are starting to get saturated with dye.

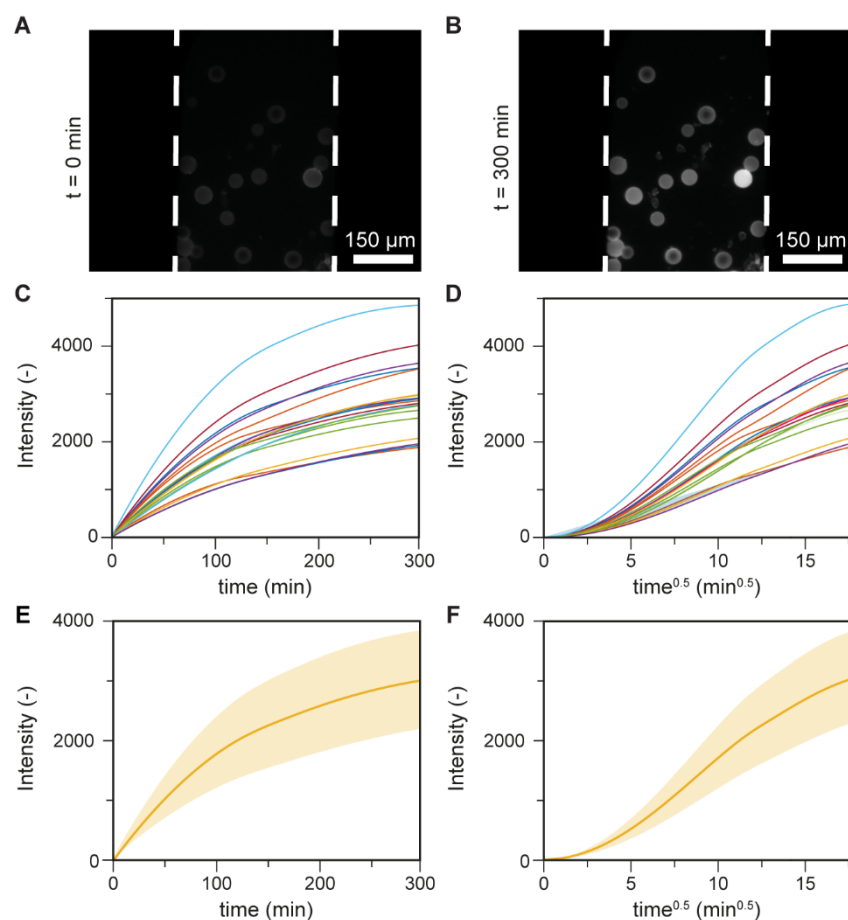


Figure 4 **A)** Zoomed-in and cropped fluorescence microscopy image of the microfluidic chamber containing silica particles with 50 nm pores at the beginning and **B)** end of the experiment. Scale bar 150 μm . **C)** Uptake curves of particles shown in Figures 4A and 4B. **D)** Uptake curves are linearized when plotted over $t^{0.5}$. **E)** and **F)** show the mean uptake curves obtained from the ones in Figures **C)** and **D)**. The shaded area represents the standard deviation of all particles considered ($n=18$).

Apart from varying the pore size of the particles to compare the uptake rates, we evaluated how the guest-host electrostatic interactions reflected upon the overall uptake process. These were tuned by using solutions at different ionic strength or pH. The pH affected the charge of the dye⁷¹ and the pore-wall surface charge density, but its fluorescence properties remained unchanged (Figure S7). In the case of silica higher pH results in more negative surface charge density⁷². The ionic strength of the solution influences the extent of the electrical double layer (EDL), a region where the liquid is not electroneutral because it contains a high concentration of counter-ions attracted by an oppositely charged surface⁷³. If the characteristic length of the EDL (commonly called the Debye length) is greater than the pore radius, there is an overlap between EDLs extending from opposite surfaces in the pores (schematically shown in Figure 5C), which slows down or even prevents the entrance of (probe) molecules with the same charge as the counter-ions due to electrostatic repulsion.

We performed experiments using three different solutions: 1. pH = 4.3, 2. pH = 4.3, and 0.01M NaCl as supporting electrolyte,

and 3. pH = 7 (Figures 5 C, 5D, and 5E). Solution 1 and 2 have the same pH but different ionic strengths ($1.3 \cdot 10^{-4}$ and $9.4 \cdot 10^{-3}$ mol/L, respectively) which translate into different Debye lengths (26 nm in solution 1 and 3 nm in solutions 2 and 3) (see SI 8). On the other hand, solutions 2 and 3 have the same ionic strength (Debye length), but different pH. The solutions used in the experiments have a pH above the silica isoelectric point (pH~2)⁷⁴. Therefore, the oxide surface hydroxyls are deprotonated and the silica surface is negatively charged⁷⁵. For all solutions, the uptake speed increased as a function of pore size and they all seem to be affected by external mass transfer as they show a non-linear regime at low $t^{0.5}$ values (Figures 5F, 5G, and 5H). However, mass transfer varied dramatically for the different conditions. Solution 1 (pH = 4.3) displayed the slowest uptake, with its linearized curve not reaching an inflection point and showing only small differences between samples with different pore sizes (Figure 5F). The linearized uptake curve of solution 2 (pH = 4.3, and 0.01M NaCl) reached the inflection point, showing moderate differences based on pore size (Figure 5G). Solution 3 (pH = 7) proved to be the fastest with respect to uptake and showed signs of saturation (i.e., the linearized uptake curve surpassed its inflection point) and the largest differences between the different porous silica samples (Figure 5H).

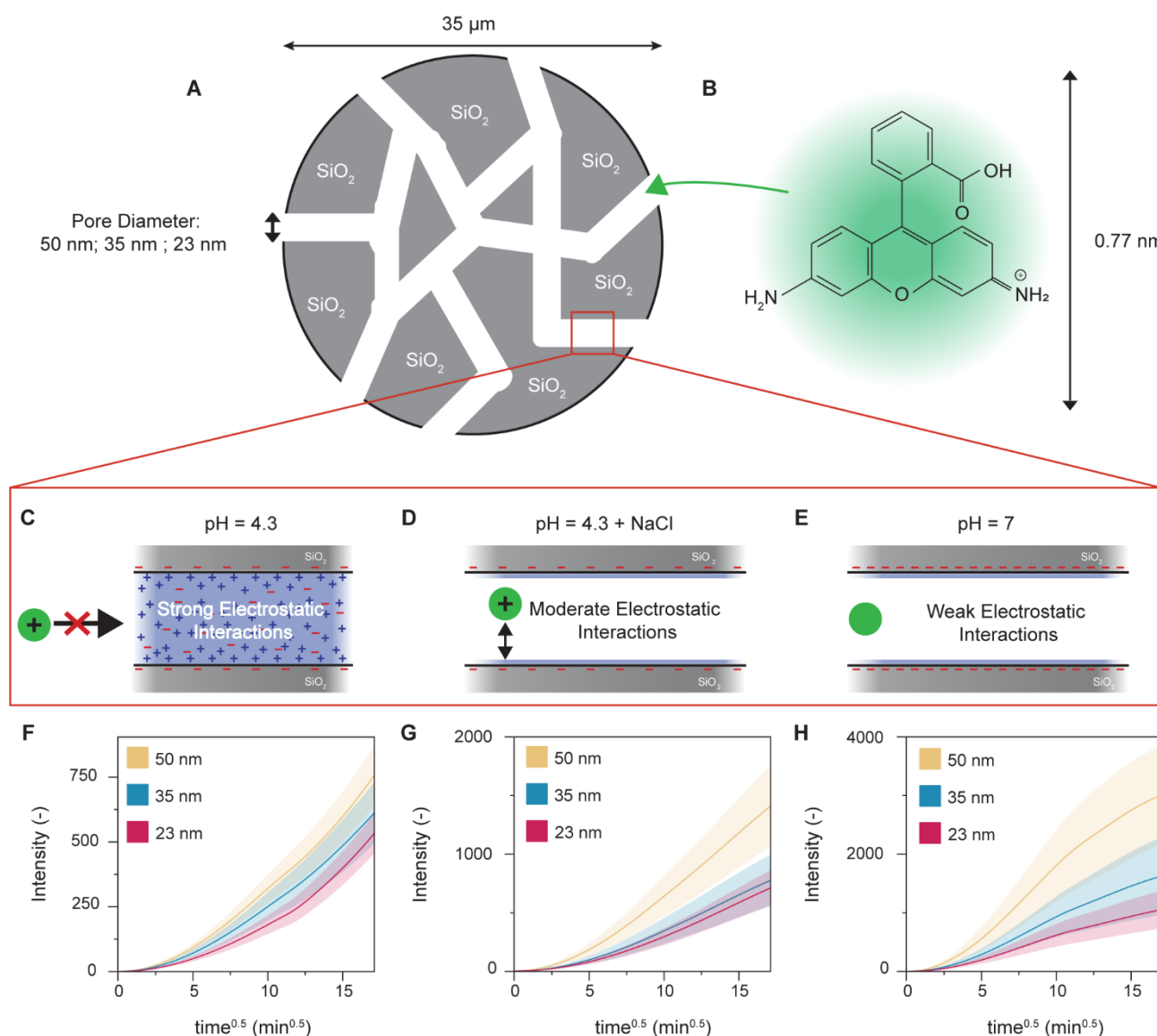


Figure 5 **A**) Silica particles (diameter: 35 μm) with almost uniform pore size distributions. Three pore sizes were used: 50, 35, and 23 nm. **B**) Rh110 chemical structure. Rh110 has a hydrodynamic diameter of 0.77 nm and is positively charged when solved in water⁷⁹. **C-E**) Schematic of electrostatic interactions between Rh110 and the negatively charged pore-walls under different conditions. **C**) pH = 4.3: A cationic electric double layer overlap (blue-shaded area) is present inside the pore which repulses the Rh110(+). **D**) pH = 4.3 and 0.01M NaCl: Increasing the ionic strength reduces the Debye length and creates a neutrally charged region within the pore that allows Rh110(+) to enter the pore more easily. **E**) pH = 7: The surface charge density of the pore walls is more negative. However, Rh110(\pm) is neutrally charged so no main probe-wall electrostatic interactions are present. **F, G, H**) Uptake curves corresponding to the conditions described in C, D, and E, respectively. Decreasing the electrostatic interactions has 2 effects on the uptake curves: it speeds up the process and it also increases the differences between samples as the pore size gradually becomes more relevant (note the difference in the y-axis scale).

This behavior can be explained by the electrostatic interactions of the different systems: solution 1 (pH = 4.3) causes Rh110 and silica to be positively⁷¹ and negatively charged⁷⁴ respectively. Moreover, due to the low ionic strength of the system, an overlapping EDL (Debye length: 26 nm > r_{pore}) predominantly containing cations is formed in the vicinity of the pore walls, which interacts with the incoming Rh110(+) repulsively, slowing the diffusion process down (Figures 5C and 5F). Solution 2 (pH = 4.3, and 0.01M NaCl), with higher ionic strength, results in a smaller Debye length (3 nm) leading to milder repulsive electrostatic interactions between the EDL and the guest molecules as well as faster mass transport (Figures 5D and 5G). Similar Debye length effects of pore diffusion have been reported previously⁷⁶⁻⁷⁸. Solution 3 (pH = 7) has the same ionic strength as solution 2 (pH = 4.3, and 0.01M NaCl) and therefore a comparable Debye length. Moreover, at pH = 7, while silica has a higher negative surface density⁷², Rh110 forms zwitterions due to the deprotonation of the carboxyl group and the amino group carries a positive charge⁷¹. Therefore, the guest-host electrostatic interactions are the lowest in this case, which results in a faster uptake and saturation (Figures 5E and 5H). As the strength of electrostatic interactions decreases (Figures 5C, 5D, and 5E), the pore size and structure become more dominant for the uptake process. This explains why we observe small, moderate, and large uptake differences between pore sizes in solutions 1, 2, and 3, respectively, in our experiments (Figures 5F, 5G, and 5H).

Figure 6A shows the obtained accessibility index distribution for different particles and wall-probe electrostatic interactions. The accessibility was evaluated from the slope of the uptake curve inflection point tangent (SI 9, Figure S8). It is worth mentioning that this analysis approach cannot be used if the first derivative of the uptake curve does not reach a maximum during the experiment (i.e., the curve has no inflection point). The experiments performed with solution 1 (pH = 4.3) do not meet this criterion and cannot be analyzed in this fashion. As qualitatively described by the uptake curves, the accessibility index decreases with pore size, and the differences are more pronounced for solution 3 (weak electrostatic interactions). The difference between 35 nm and 23 nm for solution 2 (moderate electrostatic interactions) falls within the error bar of the measurement. At pH = 7 (weak electrostatic interactions), however, the measurement remains sensitive to these differences. Therefore, by suppressing the probe-wall electrostatic interactions, it is possible to probe accessibility as dominated by the pore structure (pore size and shape). This becomes clear if one compares the accessibility index distribution at pH = 7 (Figure 6B) with the pore size distribution obtained with N₂ physisorption (Figure 6C). Note that both distributions show a significant overlap of the 35 nm sample with both the 23 nm and the 50 nm samples. Further, the relative peak positions are similarly distributed with respect to each other.

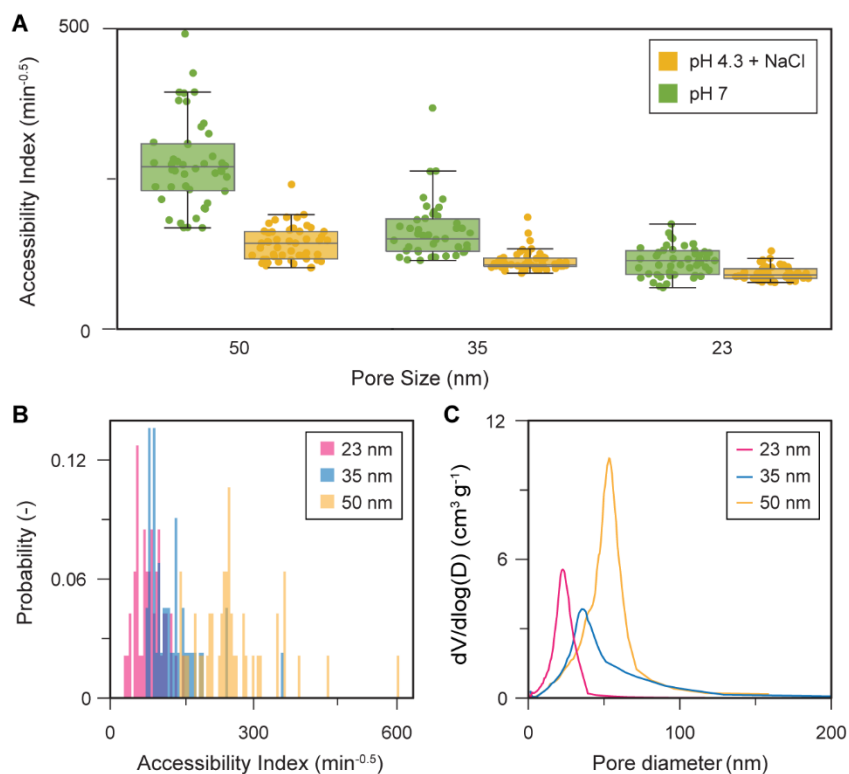


Figure 6 **A)** Comparison of accessibility index distribution of silica particles with different pore sizes (50, 35, and 23 nm) obtained by performing the experiments with fluorescent solutions at different pH but with the same ionic strength. The number of particles analyzed is ~ 50. At pH 7 the accessibility was higher as there are less electrostatic interactions. **B)** The accessibility index distribution at pH=7 and **C)** the pore size distribution exhibit similarities in terms of relative peak positions and overlapping features. The pore size distribution was determined through N₂-physisorption measurements, using Barrett-Joyner-Halenda (BJH) analysis of the desorption branch. The BET surface areas were ~ 523 m²/g (23 nm sample), ~ 439 m²/g (35 nm sample), and ~ 344 m²/g (50 nm sample). **C)** the pore size distributions obtained from N₂-physisorption.

To investigate the adsorption behavior of the system, the fluorescence of individual particles was measured and compared after two weeks of uptake, to ensure that saturation was reached (Figure 7). For all evaluated conditions, the same trend could be observed for the pore size: the equilibrium intensity, and therefore the equilibrium concentration increases as the pore size decreases. All model particles have roughly the same total porosity (~30%). If the total porosity is constant, the surface area available for adsorption decreases as a function of pore size. This explains why the amount of adsorbed Rh110 increases when particles with smaller pores are probed – intensity therefore directly correlates with surface area (BET results, SI 4). Nevertheless, the amount of adsorbed Rh110 also seems to depend strongly on the conditions used for the experiment. Interestingly, when Rh110 is neutrally charged (pH = 7, solution 3), the saturation intensity values are the lowest even though these conditions showed the fastest diffusion (Figure 5H and Figure 6A). This can be explained by the weak attractive electrostatic interactions between the probe and the walls. On the other hand, in the case of solution 1 (pH = 4.3), Rh110 and the silica walls have opposite charges, which results in a higher amount of probe electrostatically adsorbed on the walls after reaching equilibrium. Despite the repulsive electrostatic interactions between the EDL and Rh110 that slow diffusion down (Figure 5F), after long time periods, the Rh110 molecules eventually cross the predominantly positively charged EDL and adsorb on the negatively charged pore walls. If the Debye length is reduced by adding salt (solution 2, pH = 4.3 + NaCl), the interactions with the EDL are substantially reduced and the uptake is accelerated (Figure 5G). Interestingly, the final amount of adsorbed species in this case is even larger than for solution 1 (pH = 4.3). We assume that this is because some regions of the pore space of the particles remain inaccessible when a large EDL is present. This would be the case for regions connected through narrow bottle-necks where the EDL overlap is the highest, impeding Rh110 to access the whole particle void volume. Compared to N₂-physisorption which provides a single BET-surface area for an ensemble of particles, our method, on the other hand, delivers individual particle information. Furthermore, N₂-physisorption provides the accessible surface area under specific (inert) conditions, while our method can be applied under varying probe-host electrostatic interactions and is sensitive to them. This could be potentially exploited to determine the accessible surface area for a specific guest molecule (e.g., differently sized molecules within a catalyst particle). Moreover, the porous silica particles used in this study are, as mentioned above, commonly impregnated with metallocenes as active centers and used as olefin polymerization catalysts⁸⁰. The chemosensitivity of our effective surface area measurements could be used to characterize silica support particles regarding their impregnation potential.

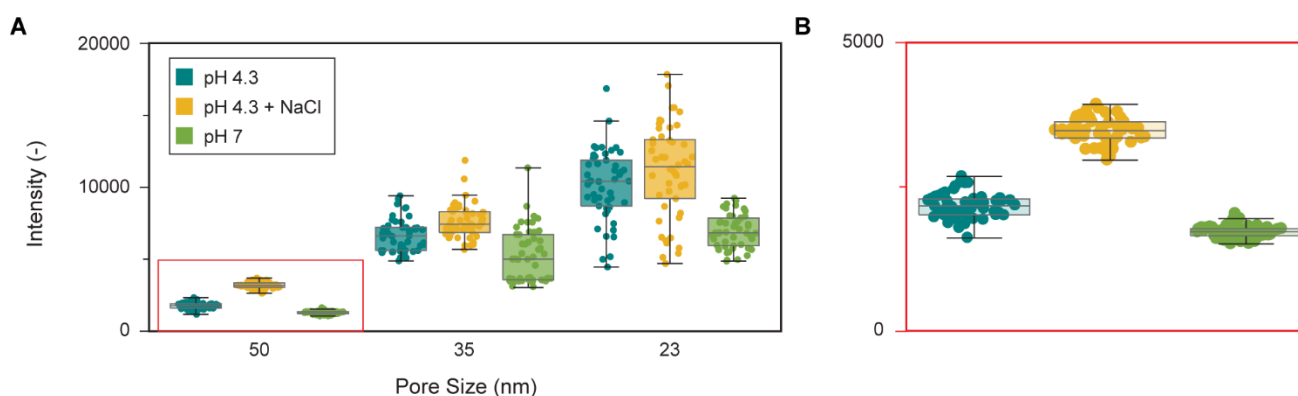


Figure 7 A) Distribution of mean fluorescent intensities of the silica model particles under different conditions after reaching saturation. Smaller pores result in higher saturation intensities, as they imply larger surface areas. At pH = 7, the equilibrium concentrations are the lowest since Rh110(±) is neutrally charged and less attracted to the silica walls. At pH 4.3 silica(-) and Rh110(+) have opposite charges resulting in higher saturation concentrations. Adding salt to the pH = 4.3 solution decreases the Debye length to the point where there is no EDL overlap. Pores connected through narrow bottle-necks with high EDL overlap become accessible as the pore entrance is no longer fully occupied by positively charged ions. Therefore, the total accessible porosity increases compared to the case of pH 4.3. As a result, the available surface area and the saturation concentrations increase as well. **C)** Zoom-in of red rectangle in **B)**. The box plots display the median, the lower and upper quartiles as well as non-outlier minima and maxima.

CONCLUSIONS

A novel analytical method to study the accessibility of individual porous particles in a high-throughput fashion was proposed and showcased using reference silica particles. From the conducted experiments, the following conclusions could be drawn: 1) Particles from the same batch showed great heterogeneity in terms of accessibility and number of accessible adsorption sites, which could not have been resolved with traditional bulk analytical methods. 2) The probe-wall electrostatic interactions proved to be of paramount importance for mass transfer and adsorption within mesoporous materials. 3) Therefore, conditions where these interactions are suppressed were employed to probe particles' accessibility as dominated by porosity. The pore-size probing sensitivity of our approach was similar to the one obtained with N₂-physisorption. 4) Evaluating the saturation intensities

proved to be suitable for studying surface area at the single particle level. Contrary to gas-physorption methods, where the results are independent of the surface chemistry, our method can be used to study the changes in accessible surface area as a function of the probe-host interactions, which could be used to study catalyst support impregnation. 5) Two linearized uptake curve parameters were found to be relevant for this kind of experiment: the accessibility index and the saturation intensity. The y-axis intercept, typically reported in mass transfer studies, proved to be redundant, as it strongly correlated with the accessibility index. Our validated method should be used to conduct uptake experiments using different probes and complex porous materials. Moreover, modifications to the microfluidic device can be made in order to make it compatible with organic solvents, expanding the application to the use of hydrophobic dyes and particles.

MATERIALS AND METHODS

Chip fabrication

The microfluidic devices were obtained by standard photolithography as previously reported by Vollertsen et al.³⁷. For the fabrication of flow layers, we first used SU8 to generate rectangular channels (~48 µm high) in the areas without valves, while AZ40XT (MicroChemicals, Germany) was employed to form ~35 µm high channels with a rounded profile. For the sections with valves, such rounded channels are needed to ensure effective sealing without any leaks.

The chips were fabricated by multilayer soft lithography. A mixture of PDMS (RTV615, Permacol, The Netherlands) base and curing agent was used to form the flow (7:1 w/w base to curing agent) and control layers (20:1 w/w base to curing agent). The mixed PDMS was then degassed for an approximate duration of 2 hours. The PDMS was then degassed for ~ 2 h.

For the creation of the control layer, a PDMS layer with a thickness of approximately 30 µm was developed using spin-coating. The flow layer was obtained by directly pouring PDMS onto the mold. Both wafers were cured at 60°C for 45 min. Upon cooling, the PDMS flow layer was removed from the wafer and the inlets and outlets were obtained by using a 1 mm hole puncher. The SiO₂ particles (SUNSPERA, AGC Si-Tech Co., Ltd) were manually deposited in the chip chamber of the flow layer by using a needle (SEIRIN J-type needle No.3) and a stereomicroscope (Olympus). Due to the sticky nature of PDMS, once placed on the layer the particles don't move. After the deposition of the particles on the flow layer, it was aligned on the control wafer, and the layers were cured overnight at 60°C. The chip was cut from the wafer and a 0.75 mm biopsy puncher was used to create the control inlet. The final step consists of bonding the chip to a microscope glass slide using a plasma cleaner (model CUTE, Femto Science, South Korea).

The valves of the microfluidic chip were driven by pneumatic actuation. The channel of the control layer was filled with water and pressurized with air (1.5 bar) by solenoid valves (Festo, Netherlands), controlled via a custom LabView program.

Uptake experiments

For the uptake experiments, the chip chambers were first filled with deionized water (PURELAB flex) so that the particles were soaked in the solvent. Rhodamine 110 Chloride (Sigma Aldrich) 100 µM in deionized water was used as fluorescent solution at pH 4.3 (solution 1) and ionic strength $1.3 \cdot 10^{-4}$ mol/L. Higher ionic strength ($9.4 \cdot 10^{-3}$ mol/L) of solution 2 and 3 was obtained by adding respectively NaCl (Sigma Aldrich) 0.01M as supporting electrolyte and NaOH (Sigma Aldrich) 0.01M to adjust the pH to 7. The solutions were injected from the inlet by using a pressure pump (Fluigent, Germany) regulating the flow from a fluid reservoir to the flow layer. After that, the chambers were closed by pressurizing the valve and the chip channels were filled with a fluorescent solution of Rhodamine 110 Chloride (Sigma Aldrich) 100 µM by using a bypass channel. Once the solution was uniformly present in the channels, the chambers were opened and filled with it. For image acquisition, a fluorescence microscope (Leica DMI 5000M) equipped with a Hamamatsu ORCA-Flash4.0 camera was used with a pE300ultra LED illumination system (CoolLED, U.K.). The fluorescent dye was excited with the blue LED light (450 nm center wavelength) combined with a BGR filter cube (dichroic mirror: 510 nm). The latter features an excitation band at 495 ± 7.5 nm and emission band at 530 ± 15 nm. The images were acquired every minute using the MicroManager microscope control software⁸¹. For the pH and conductivity measures, a Mettler Toledo SevenMulti Lab Meter was used.

ACKNOWLEDGEMENTS

This work was supported by the Netherlands Center for Multiscale Catalytic Energy Conversion (MCEC), an NWO Gravitation programme funded by the Ministry of Education, Culture and Science of the government of the Netherlands. This project has received funding from the European Union's Horizon 2020 research and innovation programme under the Marie Skłodowska-Curie grant agreement No 801359. The authors thank Dr. J.J.E. Maris (Utrecht University) and Dr. Y. Ganjkanlou (Utrecht University) for the fruitful discussions and thank Masaki Inoue (AGC) for providing the silica particles.

AUTHOR CONTRIBUTIONS

Conceptualization, F.M., A.B., L.C., R.M.G., Investigation A.B., L.C., R.M.G., J.M.D., Writing – Original Draft, A.B., L.C., R.M.G., Writing – review & editing, all authors, Funding Acquisition, B.M.W., Supervision, B.M.W., W.O., M.O., F.M.

REFERENCES

1. Kärger, J. & Ruthven, D. M. Diffusion in nanoporous materials: Fundamental principles, insights and challenges. *New J. Chem.* **40**, 4027–4048 (2016).
2. Chmelik, C. & Kärger, J. In situ study on molecular diffusion phenomena in nanoporous catalytic solids. *Chem. Soc. Rev.* **39**, 4864–4884 (2010).
3. Kärger, J., Chmelik, C., Heinke, L. & Valiullin, R. A new view of diffusion in nanoporous materials. *Chemie Ing. Tech.* **82**, 779–804 (2010).
4. Connor, P. O. & NI, H. (12) United States Patent. **2**, (2004).
5. Cauda, V., Mühlstein, L., Onida, B. & Bein, T. Tuning drug uptake and release rates through different morphologies and pore diameters of confined mesoporous silica. *Microporous Mesoporous Mater.* **118**, 435–442 (2009).
6. Andersson, J., Rosenholm, J., Areva, S. & Lindén, M. Influences of Material Characteristics on Ibuprofen Drug Loading and Release Profiles from Ordered Micro- and Mesoporous Silica Matrices. *Chem. Mater.* **16**, 4160–4167 (2004).
7. Rainer, D. R., Rautiainen, E. & Imhof, P. Novel lab-scale deactivation method for FCC catalyst: Inducing realistic accessibility responses to iron poisoning. *Appl. Catal. A Gen.* **249**, 69–80 (2003).
8. Psarras, A. C., Iliopoulou, E. F., Nalbandian, L., Lappas, A. A. & Pouwels, C. Study of the accessibility effect on the irreversible deactivation of FCC catalysts from contaminant feed metals. *Catal. Today* **127**, 44–53 (2007).
9. Buurmans, I. L. C. & Weckhuysen, B. M. Heterogeneities of individual catalyst particles in space and time as monitored by spectroscopy. *Nat. Chem.* **4**, 873–886 (2012).
10. Velthoen, M. E. Z., Meeldijk, J. D., Meirer, F. & Weckhuysen, B. M. Intra- and Interparticle Heterogeneities in Solid Activators for Single-Site Olefin Polymerization Catalysis as Revealed by Micro-Spectroscopy. *Chem. - A Eur. J.* **24**, 11944–11953 (2018).
11. Buurmans, I. L. C., Ruiz-Martínez, J., Knowles, W. V van der Beek, Bergwerff, J. A., Vogt, E. T. C., Weckhuysen, B. M. Catalytic activity in individual cracking catalyst particles imaged throughout different life stages by selective staining. *Nat. Chem.* **3**, 862–867 (2011).
12. Sato, T. & Nakatani, K. Analysis of distribution and intraparticle diffusion of a fluorescent dye in mesoporous silica gel by confocal fluorescence microspectroscopy. *Anal. Sci.* **33**, 179–183 (2017).
13. Qian, Q., Ruiz-Martínez, J., Mokhtar, M., Asiri, A. M., Al-Thabaiti, S. A., Basahel, S. N., Van Der Bij, H. E., Kornatowski, J., Weckhuysen, B. M. Single-particle spectroscopy on large SAPO-34 crystals at work: Methanol-to-olefin versus ethanol-to-olefin processes. *Chem. - A Eur. J.* **19**, 11204–11215 (2013).
14. Gartmann, N. & Brühwiler, D. Controlling and Imaging the Functional-Group Distribution on Mesoporous Silica. *Angew. Chemie Int. Ed.* **48**, 6354–6356 (2009).
15. Whiting, G. T., Nikolopoulos, N., Nikolopoulos, I., Chowdhury, A. D. & Weckhuysen, B. M. Visualizing pore architecture and molecular transport boundaries in catalyst bodies with fluorescent nanoprobes. *Nat. Chem.* **11**, 23–31 (2019).
16. Gallagher, S. H., Schlauri, P., Cesari, E., Durrer, J. & Brühwiler, D. Silica particles with fluorescein-labelled cores for evaluating accessibility through fluorescence quenching by copper. *Nanoscale Adv.* **3**, 6459–6467 (2021).
17. Chmelik, C., Gläser, R., Haase, J., Hwang, S. & Kärger, J. Application of microimaging to diffusion studies in nanoporous materials. *Adsorption* **27**, 819–840 (2021).
18. Kortunov, P. Chmelik, C., Kärger, J., Rakoczy, R. A., Ruthven, D. M., Traa, Y., Vasenkov, S., Weitkamp, J. Sorption kinetics and intracrystalline diffusion of methanol in ferrierite: An example of disguised kinetics. *Adsorption* **11**, 235–244 (2005).
19. Mitchell, S., Michels, N. L., Kunze, K. & Pérez-Ramírez, J. Visualization of hierarchically structured zeolite bodies from macro to nano length scales. *Nat. Chem.* **4**, 825–831 (2012).
20. Zečević, J., Gommès, C. J., Friedrich, H., Dejongh, P. E. & Dejong, K. P. Mesoporosity of zeolite Y: Quantitative three-dimensional study by image analysis of electron tomograms. *Angew. Chemie - Int. Ed.* **51**, 4213–4217 (2012).
21. Friedrich, H., De Jongh, P. E., Verkleij, A. J. & De Jong, K. P. Electron tomography for heterogeneous catalysts and related nanostructured materials. *Chem. Rev.* **109**, 1613–1629 (2009).
22. Díaz, I., Alfredsson, V. & Sakamoto, Y. Transmission electron microscopy in formation and growth of ordered mesoporous materials. *Curr. Opin. Colloid Interface Sci.* **11**, 302–307 (2006).
23. Midgley, P. A. & Dunin-Borkowski, R. E. Electron tomography and holography in materials science. *Nat. Mater.* **8**, 271–280 (2009).
24. Gommès, C. J., Friedrich, H., Wolters, M., De Jongh, P. E. & De Jong, K. P. Quantitative characterization of pore corrugation in ordered mesoporous materials using image analysis of electron tomograms. *Chem. Mater.* **21**, 1311–1317 (2009).
25. De Winter, D. A. M., Meirer, F. & Weckhuysen, B. M. FIB-SEM Tomography Probes the Mesoscale Pore Space of an

- Individual Catalytic Cracking Particle. *ACS Catal.* **6**, 3158–3167 (2016).
26. Bossers, K. W. , Valadian, R., Zaroni, S., Smeets, R., Friederichs, N., Garrevoet, J., Meirer, F., Weckhuysen, B. M. Correlated X-ray Ptychography and Fluorescence Nano-Tomography on the Fragmentation Behavior of an Individual Catalyst Particle during the Early Stages of Olefin Polymerization. *J. Am. Chem. Soc.* **142**, 3691–3695 (2020).
 27. Liu, Y., Meirer, F., Krest, C. M., Webb, S. & Weckhuysen, B. M. Relating structure and composition with accessibility of a single catalyst particle using correlative 3-dimensional micro-spectroscopy. *Nat. Commun.* **7**, 1–8 (2016).
 28. Meirer, F. Kalirai, S., Morris, D., Soparawalla, S., Liu, Y., Mesu, G., Andrews, J. C., Weckhuysen, B. M. Life and death of a single catalytic cracking particle. *Sci. Adv.* **1**, e1400199 (2015).
 29. Veselý, M., Valadian, R., Lohse, L. M., Toppewien, M., Spiers, K., Garrevoet, J., Vogt, E. T. C., Salditt, T., Weckhuysen, B. M., Meirer, F. 3-D X-ray Nanotomography Reveals Different Carbon Deposition Mechanisms in a Single Catalyst Particle. *ChemCatChem* **13**, 2494–2507 (2021).
 30. da Silva, J. C., Mader, K., Holler, M., et al. Assessment of the 3-D pore structure and individual components of preshaped catalyst bodies by X-ray imaging. *ChemCatChem* **7**, 413–416 (2015).
 31. Mayorga-González, R., Rivera-Torrente, M., Nikolopoulos, N., Bossers, K. W., Valadian, R., Yus, J., Seoane, B., Weckhuysen, B. M., Meirer, F. Visualizing defects and pore connectivity within metal-organic frameworks by X-ray transmission tomography. *Chem. Sci.* **12**, 8458–8467 (2021).
 32. Bassim, N. D., De Gregorio, B.T., Kilcoyne, A.L.D., Scott, K., Chou, T., Wirick, S., Cody, G., Stroud, R.M. Minimizing damage during FIB sample preparation of soft materials. *J. Microsc.* **245**, 288–301 (2012).
 33. Zabilska, A., Clark, A. H., Ferri, D., Nachttegaal, M., Kröcher, O., Safonova, O. V. Beware of beam damage under reaction conditions: X-ray induced photochemical reduction of supported VO x catalysts during in situ XAS experiments. *Phys. Chem. Chem. Phys.* **24**, 21916–21926 (2022).
 34. Nieuwelink, A. E., Vollenbroek, J. C., Ferreira De Abreu, A. C., Tiggelaar, R. M., Van Den Berg, A., Odijk, M., Weckhuysen, B. M. Single catalyst particle diagnostics in a microreactor for performing multiphase hydrogenation reactions. *Faraday Discuss.* **229**, 267–280 (2021).
 35. Solsona, M., Nieuwelink, A. E., Meirer, F., Abelman, L., Odijk, M., Olthuis, W., Weckhuysen, B. M., van den Berg, A. Magnetophoretic Sorting of Single Catalyst Particles. *Angew. Chemie - Int. Ed.* **57**, 10589–10594 (2018).
 36. Broccoli, A. Vollertsen, A. R., Roels, P., van Vugt, A., van den Berg, A., Odijk, M. Nanoparticle Printing for Microfluidic Applications: Bipolar Electrochemistry and Localized Raman Sensing Spots. *Micromachines* **14**, 453 (2023).
 37. Vollertsen, A. R., De Boer, D., Dekker, S., Wesselink, B. A. M., Haverkate, R. Rho, H. S., Odijk, M. Modular operation of microfluidic chips for highly parallelized cell culture and liquid dosing via a fluidic circuit board. *Microsystems Nanoeng.* **6**, 107 (2020).
 38. Haneveld, J., Tas, N. R., Brunets, N., Jansen, H. V. & Elwenspoek, M. Capillary filling of sub- 10 nm nanochannels. *J. Appl. Phys.* **104**, (2008).
 39. Do, D. D. *Adsorption analysis: Equilibria and kinetics.* (World Scientific, 1998).
 40. Klein, G. Principles of adsorption and adsorption processes. *Reactive Polymers, Ion Exchangers, Sorbents* **4**, 62 (1985).
 41. Brandani, S. Kinetics of liquid phase batch adsorption experiments. *Adsorption* **27**, 353–368 (2021).
 42. Weber, B. W. J. Proceedings of the American Society of Civil Engineers. **89**, 31–59 (1963).
 43. Wu, F. C., Tseng, R. L. & Juang, R. S. Initial behavior of intraparticle diffusion model used in the description of adsorption kinetics. *Chem. Eng. J.* **153**, 1–8 (2009).
 44. Teixeira, R. N. P., Sousa Neto, V. O., Oliveira, J. T., Oliveira, T. C., Melo, D. Q., Silva, M. A. A., Nascimento, R. F. Study on the use of roasted barley powder for adsorption of Cu²⁺ ions in batch experiments and in fixed-bed columns. *BioResources* **8**, 3556–3573 (2013).
 45. Pholosi, A., Naidoo, E. B. & Ofomaja, A. E. Intraparticle diffusion of Cr(VI) through biomass and magnetite coated biomass: A comparative kinetic and diffusion study. *South African J. Chem. Eng.* **32**, 39–55 (2020).
 46. Ali, H. E., Nasef, S. M. & Gad, Y. H. Remediation of Astrazon blue and Lerui acid brilliant blue dyes from waste solutions using amphoteric superparamagnetic nanocomposite hydrogels based on chitosan prepared by gamma rays. *Carbohydr. Polym.* **283**, (2022).
 47. Hashem, A. & El-Khiraigy, K. Bioadsorption of Pb (II) onto Anethum graveolens from contaminated wastewater: Equilibrium and Kinetic studies. *J. Environ. Prot. (Irvine, Calif.)* **04**, 108–119 (2013).
 48. Largette, L. & Pasquier, R. A review of the kinetics adsorption models and their application to the adsorption of lead by an activated carbon. *Chem. Eng. Res. Des.* **109**, 495–504 (2016).
 49. Özcan, A. S. & Özcan, A. Adsorption of acid dyes from aqueous solutions onto acid-activated bentonite. *J. Colloid Interface Sci.* **276**, 39–46 (2004).
 50. Özcan, A. & Özcan, A. S. Adsorption of Acid Red 57 from aqueous solutions onto surfactant-modified sepiolite. *J. Hazard.*

- Mater.* **125**, 252–259 (2005).
51. Kannan, N. & Sundaram, M. M. Kinetics and mechanism of removal of methylene blue by adsorption on various carbons - A comparative study. *Dye. Pigment.* **51**, 25–40 (2001).
 52. El Mouzdahir, Y. et al. Interaction of stevensite with Cd²⁺ and Pb²⁺ in aqueous dispersions. *Appl. Clay Sci.* **35**, 47–58 (2007).
 53. Önal, Y. Kinetics of adsorption of dyes from aqueous solution using activated carbon prepared from waste apricot. *J. Hazard. Mater.* **137**, 1719–1728 (2006).
 54. Akmil-Başar, C., Önal, Y., Kiliçer, T. & Eren, D. Adsorptions of high concentration malachite green by two activated carbons having different porous structures. *J. Hazard. Mater.* **127**, 73–80 (2005).
 55. Lorenc-Grabowska, E. & Gryglewicz, G. Adsorption of lignite-derived humic acids on coal-based mesoporous activated carbons. *J. Colloid Interface Sci.* **284**, 416–423 (2005).
 56. El-Khaiary, M. I. Kinetics and mechanism of adsorption of methylene blue from aqueous solution by nitric-acid treated water-hyacinth. *J. Hazard. Mater.* **147**, 28–36 (2007).
 57. Çiçek, F., Özer, D., Özer, A. & Özer, A. Low cost removal of reactive dyes using wheat bran. *J. Hazard. Mater.* **146**, 408–416 (2007).
 58. Singh, K. K., Rastogi, R. & Hasan, S. H. Removal of cadmium from wastewater using agricultural waste 'rice polish'. *J. Hazard. Mater.* **121**, 51–58 (2005).
 59. Huo, M. X. et al. Facile synthesis of chitosan-based acid-resistant composite films for efficient selective adsorption properties towards anionic dyes. *Carbohydr. Polym.* **254**, (2021).
 60. Yang, Y., Lin, X., Wei, B., Zhao, Y. & Wang, J. Evaluation of adsorption potential of bamboo biochar for metal-complex dye: Equilibrium, kinetics and artificial neural network modeling. *Int. J. Environ. Sci. Technol.* **11**, 1093–1100 (2014).
 61. Medley, J. A. & Andrews, M. W. The Effect of a Surface Barrier on Uptake Rates of Dye into Wool Fibers. *Text. Res. J.* **29**, 398–403 (1959).
 62. Brandani, S. Kinetics of liquid phase batch adsorption experiments. *Adsorption* **27**, 353–368 (2021).
 63. Cheung, W. H., Szeto, Y. S. & McKay, G. Intraparticle diffusion processes during acid dye adsorption onto chitosan. *Bioresour. Technol.* **98**, 2897–2904 (2007).
 64. Sze, M. F. F. & McKay, G. An adsorption diffusion model for removal of para-chlorophenol by activated carbon derived from bituminous coal. *Environ. Pollut.* **158**, 1669–1674 (2010).
 65. Alexander, F., Poofs, V. J. P. & McKay, G. Adsorption Kinetics and Diffusional Mass Transfer Processes during Color Removal from Effluent Using Silica. *Ind. Eng. Chem. Process Des. Dev.* **17**, 406–410 (1978).
 66. Sun, Q. & Yang, L. The adsorption of basic dyes from aqueous solution on modified peat-resin particle. *Water Res.* **37**, 1535–1544 (2003).
 67. Özer, D., Dursun, G. & Özer, A. Methylene blue adsorption from aqueous solution by dehydrated peanut hull. *J. Hazard. Mater.* **144**, 171–179 (2007).
 68. Weber, W. J. & Morris, J. C. Closure to "Kinetics of Adsorption on Carbon from Solution". *J. Sanit. Eng. Div.* **89**, 53–55 (1963).
 69. Beija, M., Afonso, C. A. M. & Martinho, J. M. G. Synthesis and applications of rhodamine derivatives as fluorescent probes. *Chem. Soc. Rev.* **38**, 2410–2433 (2009).
 70. Gendron, P. O., Avaltroni, F. & Wilkinson, K. J. Diffusion coefficients of several rhodamine derivatives as determined by pulsed field gradient-nuclear magnetic resonance and fluorescence correlation spectroscopy. *J. Fluoresc.* **18**, 1093–1101 (2008).
 71. Blom, H., Hassler, K., Chmyrov, A. & Widengren, J. Electrostatic interactions of fluorescent molecules with dielectric interfaces studied by total internal reflection fluorescence correlation spectroscopy. *Int. J. Mol. Sci.* **11**, 386–406 (2010).
 72. Behrens, S. H. & Grier, D. G. The charge of glass and silica surfaces. *J. Chem. Phys.* **115**, 6716–6721 (2001).
 73. Sen, T. & Barisik, M. Internal surface electric charge characterization of mesoporous silica. *Sci. Rep.* **9**, 1–9 (2019).
 74. Kosmulski, M. The pH dependent surface charging and points of zero charge. VIII. Update. *Adv. Colloid Interface Sci.* **275**, 102064 (2020).
 75. Bo, Z., McCullough, L. R., Dull, S., Ardagh, M. A., Wang, J., Notestein, J. Strong electrostatic adsorption of Pt onto SiO₂ partially overcoated Al₂O₃ - Towards single atom catalysts. *J. Chem. Phys.* **151**, (2019).
 76. Plecis, A., Schoch, R. B. & Renaud, P. Ionic transport phenomena in nanofluidics: Experimental and theoretical study of the exclusion-enrichment effect on a chip. *Nano Lett.* **5**, 1147–1155 (2005).
 77. Wu, H., Wang, D. & Schwartz, D. K. Connecting Hindered Transport in Porous Media across Length Scales: From Single-Pore to Macroscopic. *J. Phys. Chem. Lett.* **11**, 8825–8831 (2020).

78. Wu, H., Sarfati, R., Wang, D. & Schwartz, D. K. Electrostatic Barriers to Nanoparticle Accessibility of a Porous Matrix. *J. Am. Chem. Soc.* **142**, 4696–4704 (2020).
79. Alemdaroglu, F. E., Wang, J., Börsch, M., Berger, R. & Herrmann, A. Enzymatic control of the size of DNA block copolymer nanoparticles. *Angew. Chemie - Int. Ed.* **47**, 974–976 (2008).
80. Bolner, F. M., Blazio, Y. R., Lara, B. R., Machado, F. & McKenna, T. F. L. Impact of silica pore structure on the performance of metallocene catalysts in ethylene gas-phase polymerization. *Can. J. Chem. Eng.* **101**, 4819–4831 (2023).
81. Edelstein, A. D., Tsuchida, M. A., Amodaj, N., Pinkard, H., Vale, R. D., Stuurman, N. Advanced methods of microscope control using µManager software. *J. Biol. Methods* **1**, e10 (2014).